Measuring the Orbital-Angular-Momentum Complex Spectrum of Light with the Fast Fourier Transform

Jialong Zhu,[1,2] Yihua Wu,[1] Le Wang,[1] Hailong Zhou,[3,*] and Shengmei Zhao[1,4,5,†]

[1] *Institute of Signal Processing and Transmission, Nanjing University of Posts and Telecommunications (NUPT), Nanjing 210003, China*

[2] *School of Information Engineering, Suqian University, Suqian 223800, China*

[3] *Wuhan National Laboratory for Optoelectronics, School of Optical and Electronic Information, Huazhong University of Science and Technology, Wuhan 430074, China*

[4] *Key Lab of Broadband Wireless Communication and Sensor Network Technology (Nanjing University of Posts and Telecommunications), Ministry of Education, Nanjing, China*

[5] *National Laboratory of Solid State Microstructures, Nanjing University, Nanjing 210093, China*

(Received 29 December 2022; revised 11 May 2023; accepted 14 June 2023; published 7 July 2023)

Measuring the orbital-angular-momentum (OAM) complex spectrum of light is very important in OAM-based applications. In this paper, we propose and experimentally demonstrate a simple scheme to measure the OAM complex spectrum of light with the fast Fourier transform (FFT). The light with input OAM modes coaxially interferes with a Gaussian light beam that is generated locally to achieve the intensity distribution of the interference. By subtracting the intensity distribution of the input OAM light from this interference intensity distribution, the OAM complex spectrum can be extracted by employing the FFT transform on the result of the subtraction. In addition, we also present an approach to enlarge the range of detectable OAM modes (from 1 to 50) and analyze the effects of optical alignment and the number of superimposed OAM modes on the measurement results. The proposed scheme is demonstrated in a proof-of-principle experiment, where six superimposed OAM modes can be measured without error, with their average deviation of amplitude and phase being 0.07 and 0.308, respectively. The proposed scheme can exploit applications in some advanced domains, including OAM sensing, OAM imaging, optical communication decoding, and various other OAM-based systems.

DOI: 10.1103/PhysRevApplied.20.014010

I. INTRODUCTION

In 1992, Allen *et al.* proposed that a vortex beam could carry orbital angular momentum (OAM), which is characterized by $\exp(il\theta)$, where θ is the azimuthal angle and l is the topological charge (TC) [1–4]. Superimposed OAMs of light, due to a helical wavefront being an independent physical dimension, have been used to multiplex a wide range of OAM TCs [5]. According to their orthogonality and selectivity, OAMs have wide optical applications in optical communications [6,7], quantum information processing [8–10], and as optical sensors [11,12], etc. In OAM applications, when the complex coefficients (amplitude and phase) of the superimposed OAMs are known, the complete spatial distribution of the electric field can be obtained and significant properties such as beam quality factor M^2, beam width, and wavefront are easily computed at any propagation distance [13,14]. Hence, measuring the OAM complex spectrum is essential in OAM-based applications.

Recent years have witnessed the development of measurement of the OAM complex spectrum. Compared with measuring a single OAM TC, measuring superimposed OAM modes is not a trivial task, but several schemes have been proposed, which can typically be divided into interference-based spectrum measurement [15–21], coordinate transformation [22–25], and machine learning [26,27]. For interference-based spectrum measurement, the superimposed OAM beam is interfered with a known beam, and then the OAM spectrum is measured from the interference results [15–21]. In terms of coordinate transformation, the superimposed OAMs are sorted into different spatial locations [22–25]. For the machine-learning method, a neural network combined with a phase-only diffraction optical element is employed to measure the intensity distribution of the OAM spectrum [26,27].

In our previous work, we employed the rotational Doppler effect to measure the power and phase distributions of superimposed OAMs simultaneously [28]. There

*hailongzhou@hust.edu.cn
†zhaosm@njupt.edu.cn

are some other methods to measure the OAM complex spectrum, such as spatial mode decomposition [29,30], time mapping [31,32], and grayscale algorithm [33], etc. However, using the fast Fourier transform (FFT) to measure the input OAM complex spectrum with superimposed modes has been less discussed.

In this paper, we present a new scheme for measuring the complex spectrum of orbital angular momentum using the fast Fourier transform. In our proposed scheme, the input superimposed OAM modes of light are coaxially interfered with a Gaussian light beam, yielding an interference intensity distribution. By subtracting the intensity distribution of the input superimposed OAM light from the interference distribution, the OAM complex spectrum can be obtained via FFT. To enhance the accuracy of measuring the complex coefficients (amplitude and phase) of OAM modes, we introduce a calibration method. Additionally, we propose an approach to expand the detectable range of OAM TCs. Similar to the telecommunication decoding system, our scheme shows significant potential for use in OAM complex spectral analysis and measurement for OAM-based communication systems with mode-division multiplexing.

Compared to our previous approach employing the rotational Doppler effect [28], the proposed new scheme offers two main advantages. Firstly, it simplifies the complexity of the measurement apparatus, so as to reduce errors. Secondly, the measurement efficiency is improved. The proposed scheme requires only two intensity images captured by a camera to complete the measurement, whereas the previous approach required the camera to continuously capture intensity images over a period of time to complete the measurement.

II. METHODS

The proposed measurement scheme can be depicted as shown in Fig. 1. Figure 1(a) displays a schematic diagram of the proposed scheme, while Fig. 1(b) presents the OAM-primitive pattern, OAM-interferential pattern, and OAM-measuring pattern, which are the results of two superimposed OAM modes with $l = 3, 8$. The process to obtain the complex spectrum by applying the FFT transform on the OAM-measuring pattern is demonstrated in Fig. 1(c).

The superimposed OAM beams with input TC values in Fig. 1(a) can be denoted as

$$E_1 = \sum_{n=1}^{N} A_{l_n,r} \exp[i(l_n\theta + \phi_{l_n})], \tag{1}$$

where N and r denote the total number of input superimposed OAM modes and the measurement radius, respectively. The nth OAM TC value is represented by l_n, while A_{l_n} and ϕ_{l_n} denote the superimposed amplitude and initial phase of the nth OAM mode, respectively. The superimposed amplitude can be expressed as

$$A_{l_n,r} = a_{l_n} G_{l_n,r}, \tag{2}$$

where a_{l_n} represents the initial amplitude of the nth OAM mode, and $G_{l_n,r} = r^{2|l_n|}e^{-2r^2}$ denotes the amplitude calibration coefficient of the Laguerre-Gaussian mode with the measurement radius [34].

From Fig. 1(a), when the input OAM beam passes through a beam splitter (BS1) and is detected by the charge-coupled device (CCD1), the initial phase of the beam is significantly affected by the transmission distance z and factors associated with l [35], which can be expressed as

$$\Phi_{l_n,z} = \phi_{l_n} + P(l,z), \tag{3}$$

where $P(l,z)$ is the phase calibration coefficient. Because of the complexity of the measurement system (transmission ratio and reflection ratio), the amplitude and phase calibration coefficients can be obtained through prior experiments. The intensity of the input OAM beam is recorded by CCD1, named OAM-primitive pattern, which should be described as

$$I_1(\theta,r) = \sum_{n=1}^{N} \left|A_{l_n,r}\right|^2 + 2 \sum_{N\geq p\geq q\geq 1} \left|A_{l_p,r}A_{l_q,r}\right| \cos(\Delta l_{pq}\theta + \Delta\Phi_{pq}), \tag{4}$$

where $\Delta l_{pq} = l_p - l_q$ and $\Delta\Phi_{pq} = \Phi_{l_p,z} - \Phi_{l_q,z}$ represent the OAM mode difference and phase difference between the pth and qth OAM components, respectively; and $|\cdot|$ represents the absolute value function. The collected intensity in Eq. (4) consists of two terms, a direct current term and a cross term between the different input OAM modes. The cross term can be seen as the harmonics.

On the other hand, the reference Gaussian beam can be given briefly as

$$E_2 = a_{\text{ref}}(r) \exp(i\phi_{\text{ref}}), \tag{5}$$

where $a_{\text{ref}}(r)$ and ϕ_{ref} represent the amplitude and the phase of the Gaussian beam, respectively. The amplitude of $a_{\text{ref}}(r)$ is dependent on r and follows a Gaussian distribution. The input OAM beam is reflected through BS1 to BS2 and interferes coaxially with the reference Gaussian beam. The resulting OAM-interferential pattern captured

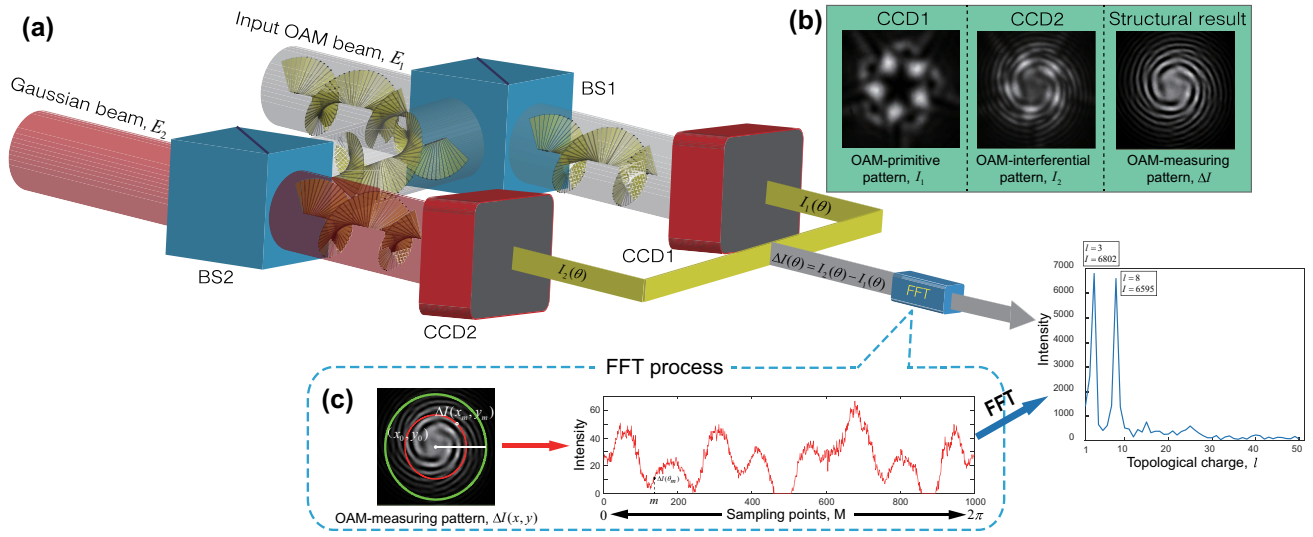

FIG. 1. The principle of the proposed scheme. (a) A schematic diagram of the proposed scheme. (b) The input OAM beam is set to $l = 3, 8$, and their OAM-primitive pattern, OAM-interferential pattern, and OAM-measuring pattern. (c) The process of implementing the FFT of OAM-measuring pattern.

by CCD2 can be expressed as

$$\begin{aligned} I_2(\theta, r) &= (E_1 + E_2)(E_1 + E_2)^* \\ &= |a_{\text{ref}}(r)|^2 + \sum_{n=1}^{N} \left|A_{l_n,r}\right|^2 \\ &\quad + 2 \sum_{N \geq p \geq q \geq 1} \left|A_{l_p,r} A_{l_q,r}\right| \cos(\Delta l_{pq}\theta + \Delta\Phi_{pq}) \\ &\quad + 2 \sum_{n=1}^{N} |a_{\text{ref}}(r)| \left|A_{l_n,r}\right| \cos(l_n\theta + \Phi_{l_n,z} - \phi_{\text{ref}}). \end{aligned} \tag{6}$$

The intensity recorded in Eq. (6) is composed of three terms: a direct current term, a cross term, and an object term that contains the OAM mode (l_n), amplitude ($A_{l_n,r}$), and phase ($\Phi_{l_n,r}$). The OAM-measuring pattern [shown in Fig. 1(b)] is generated by subtracting the OAM-primitive pattern from the OAM-interferential pattern, and can be given as

$$\begin{aligned} \Delta I(\theta, r) &= I_2(\theta, r) - I_1(\theta, r) \\ &= |a_{\text{ref}}(r)|^2 \\ &\quad + 2 \sum_{n=1}^{N} |a_{\text{ref}}(r)| \left|A_{l_n,r}\right| \cos(l_n\theta + \Phi_{l_n,z} - \phi_{\text{ref}}). \end{aligned} \tag{7}$$

Here, the cross term and partial direct-current term are removed. The expression in Eq. (7) is similar to the traditional electromagnetic signal expression form.

Then, an FFT with respect to θ is operated on $\Delta I(\theta)$, resulting in the OAM complex spectrum ($T(l, r)$),

$$\Delta I(\theta, r) \xrightarrow{\text{FFT}(\theta)} T(l, r). \tag{8}$$

The azimuthal angle (θ) is sampled and the total sampling number is M. The azimuthal angle θ can be described as $\theta_m = (2\pi/M)m$. According to the Nyquist theorem [36], the total sampling number (M) is assumed to be greater than twice the maximum OAM mode ($l_{\max}$) (i.e., $M \geq 2l_{\max}$).

The detailed mathematical process of obtaining the OAM complex spectrum can be described as

$$\begin{aligned} T(l, r) &= \sum_{m=0}^{M-1} \Delta I(\theta_m) e^{-il\theta_m} \\ &= \sum_{m=0}^{M-1} \left[2 \sum_{n=1}^{N} |a_{\text{ref}}(r)| \left|A_{l_n,r}\right| \cos(l_n\theta_m + \Phi_{l_n} - \phi_{\text{ref}}) \right] \\ &\quad e^{-il\theta_m}. \end{aligned} \tag{9}$$

According to Euler's formula, the cosine function can be described as

$$\begin{aligned} &\cos(l_n\theta_m + \Phi_{l_n} - \phi_{\text{ref}}) \\ &= \tfrac{1}{2}(e^{i(l_n\theta_m + \Phi_{l_n} - \phi_{\text{ref}})} + e^{-i(l_n\theta_m + \Phi_{l_n} - \phi_{\text{ref}})}). \end{aligned} \tag{10}$$

Substituting Eq. (10) into Eq. (9) and selecting a known measurement radius (r_0), the OAM complex spectrum

$(T(l))$ can be given by

$$T(l) = \sum_{n=1}^{N} \left\{ |a_{\mathrm{ref}}(r_0)| \sum_{m=0}^{M-1} \left| A_{l_n,r_0} \right| e^{i(\Phi_{l_n} - \phi_{\mathrm{ref}})} e^{i(l_n - l)\theta_m} \right\}$$
$$= 2\pi\, |a_{\mathrm{ref}}(r_0)| \sum_{n=1}^{N} \left| A_{l_n,r_0} \right| e^{i(\Phi_{l_n} - \phi_{\mathrm{ref}})} \delta(l - l_n), \quad (11)$$

where $\delta(l - l_n)$ represents an impulse function and its meaningless mirror function $(\delta(l + l_n))$ is not shown in Eq. (9).

From Eq. (11), the initial amplitude and phase of the OAM modes can be measured as

$$a'_{l_n} = \frac{|T(l, r_0)|}{2\pi\, |a_{\mathrm{ref}}(r_0) G'_{l_n,r_0}|},$$
$$\phi'_{l_n} = \arctan\left(\frac{\mathrm{Im}(T(l, r_0))}{\mathrm{Re}(T(l, r_0))} \right) + \phi_{\mathrm{ref}} - P'(l, z). \quad (12)$$

Here $\arctan(\cdot)$ represents the inverse tangent function; $\mathrm{Im}(\cdot)$ and $\mathrm{Re}(\cdot)$ represent the imaginary component and the real component of the OAM complex spectrum $(T(l, r_0))$, respectively; and G'_{l_n,r_0} and $P'(l, z)$ represent the measured amplitude and phase calibration coefficient in the prior experiment. The effects of transmission ratio, reflection ratio, and CCD response time on the measurement results are eliminated by the prior calibration experiments. This involves selecting a measurement radius (r_0) and setting the initial amplitude and phase of each OAM mode to $a_{l_n} = 1$ and $\phi_{l_n} = 0$, respectively. Under the same experimental conditions, each individual OAM mode with TC ranging from 1 to N was measured separately. From the measurement results, the amplitude calibration coefficient (G'_{l_n,r_0}) and phase calibration coefficient $(P'(l, z))$ are obtained.

In the following, we design an algorithm to realize the FFT with respect to θ on $\Delta I(\theta)$. The main steps of this algorithm are shown in Fig. 1(c) and listed below.

(i) Firstly, a single OAM mode is adopted to locate the central position (x_0, y_0). Because its OAM-primitive pattern is a ring-shaped pattern (doughnut), it is easy to find out the center position (x_0, y_0). Then, adjust the reference beam and determine the radial alignment by observing whether petal-like speckles are produced in the OAM-interferential pattern.

(ii) The second step is to extract the intensity values on the red ring. The relationships between the pixel location (x_m, y_m) in the OAM-measuring pattern and (θ_m, r) are

$$x_m = x_0 + r\cos(\theta_m),$$
$$y_m = y_0 + r\sin(\theta_m), \quad (13)$$

where $r = 1, \ldots, R$, and R represents the total radius of the measurement bound.

(iii) The third step is to determine the measurement bound. The sum of the intensity values of a circle is calculated, which can be given as

$$\Delta I_{\mathrm{cir}}(r) = \sum_{m=0}^{M-1} \Delta I(x_m, y_m). \quad (14)$$

The threshold value (I_{thr}) is set to determine the measurement bound. In Fig. 1(c), the green ring, $\Delta I_{\mathrm{cir}}(R) = I_{\mathrm{thr}}$, is the measurement bound. The intensity information outside the measurement bound (green ring) is too weak to be available.

(iv) Finally, half of the measurement bound $(r_0 = R/2)$ is normally used to extract the intensity distribution, which is the red ring in the OAM-measuring pattern [Fig. 1(c)]. The intensity distribution in polar coordinates is converted into the intensity signal in Cartesian coordinates. Then, the OAM spectrum is obtained by using the FFT on the intensity signal. Note that, according to Eq. (11), the OAM modes (l) are not dependent on the radius (r), and the measurement experiment can be completed using a single measurement radius.

To evaluate the measurement accuracy, we define the average deviations of amplitude and phase as

$$\delta_a = \frac{1}{N} \sum_{n=1}^{N} |a_{l_n} - a'_{l_n}|,$$
$$\delta_\phi = \frac{1}{N} \sum_{n=1}^{N} |\phi_{l_n} - \phi'_{l_n}|. \quad (15)$$

Here δ_a and δ_ϕ represent the average deviation of amplitude and phase, respectively; a_{l_n} and ϕ_{l_n} are the theoretical values; and a'_{l_n} and ϕ'_{l_n} are the experimental values.

III. EXPERIMENTAL RESULTS

A. Experimental setup

A proof-of-principle experiment is designed to demonstrate the proposed scheme. Figure 2 shows the experimental setup. A He-Ne laser beam with a wavelength of 632.8 nm is split into the signal and reference beams by beam splitter BS1. The signal beam is then directed through beam splitter BS2 and onto a spatial light modulator (SLM), a Holoeye PLUTO-2-VIS. The SLM imprints an OAM multiplexing hologram onto the signal beam, which can be generated via the superposition of different OAM single holograms. The reflected beam from the SLM can be used to emulate an input OAM beam. The input OAM beam is reflected by beam splitters BS2 and BS3 and is then coaxially interfered with the reference beam.

The transmission direction of the reference beam is adjusted using a mirror, and the intensity of the Gaussian beam is adjusted using a variable neutral density filter

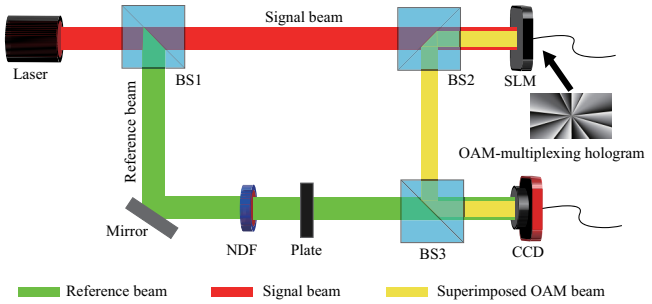

FIG. 2. The experimental setup.

(NDF). By controlling the NDF, the intensity of the Gaussian beam can be matched with that of the signal beam. The plate here is used to generate the OAM-primitive pattern or the OAM-interferential pattern by the same experimental setup. When the plate is used, the Gaussian beam is blocked and only the input OAM beam is collected by the CCD camera, and the OAM-primitive pattern is obtained. When the plate is removed, the Gaussian beam can coaxially interfere with the input OAM beam, and the OAM-interferential pattern is obtained. It is important to note that the CCD camera converts light intensity into gray values ranging from 0 to 255. The total sampling number is set to 1000 ($M = 1000$), which means that the sampling interval of the angle is $\Delta\theta = 2\pi/1000$.

B. Measurement of OAM modes and amplitude spectrum

To verify the feasibility of the proposed measurement scheme, assume that the TCs of the input OAM modes are limited to a range, say from 1 to 15. In the prior experiment, we first select a measurement radius of $r_0 = 150$ pixels and scan the input OAM modes from OAM-1 to OAM-15 to obtain the measurement amplitude calibration coefficient ($G'_{l_n,r}$) and measurement phase calibration coefficient ($P'(l,z)$), which are shown in Fig. 3(a) and Fig. 3(b), respectively.

The measuring results are presented in Fig. 4. Figure 4(a) illustrates the measurement process of the OAM amplitude spectrum when the input OAM modes consist of

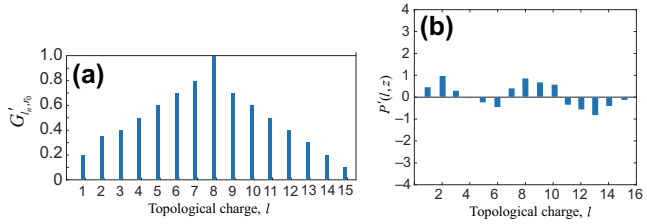

FIG. 3. The calibration coefficient in $r_0 = 150$ pixels. (a) The measurement amplitude calibration coefficient (G'_{l_n,r_0}). (b) The measurement phase calibration coefficient ($P'(l,z)$).

two modes ($l = 3, 8$). Figure 4(b) shows the measurement process of the OAM amplitude spectrum when the input OAM modes consist of three modes ($l = 2, 4, 6$). Finally, Fig. 4(c) shows the measurement process of the OAM amplitude spectrum when the input OAM modes consist of six modes ($l = 2, 4, 6, 8, 10, 13$).

In the two-modes experiment, the initial amplitudes of OAM modes with $l = 3, 8$ are set to $a_{l_n} = 1, 1$. From Fig. 4(a), the OAM-measuring pattern can be obtained from the OAM-interferential pattern minus the OAM-primitive pattern. The intensity distribution is sampled and converted into the intensity distribution with Cartesian coordinates. By FFT, the OAM amplitude spectrum can be obtained. According to Eq. (12), the initial amplitude distribution can be recovered by using the OAM amplitude spectrum over the amplitude calibration coefficients (G'_{l_n,r_0}) and the amplitude of the reference beam ($a_{\mathrm{ref}}(r_0)$), which are $a'_{l_1} = 0.970$ and $a'_{l_2} = 0.974$. The other OAM modes have values in the initial amplitude distribution, which are mainly due to harmonics. The fluctuation range of harmonics is 0.11 ± 0.06, which is obtained by experimental statistics. Hence, the threshold is set to $a_{\mathrm{thr}} = 0.3$ for filtering out the object OAM modes. Overall, our proposed scheme can accurately measure the OAM modes and their amplitude from the measurement results. The average deviation of the measured amplitude is $\delta_a = 0.028$, demonstrating the high precision of our scheme.

Similarly, in the three-modes experiment, the initial amplitude of OAM modes with $l = 2, 4, 6$ are set to $a_{l_n} = 1, 1, 1$. From Fig. 3(b), the initial amplitude distribution can be obtained ($a'_{l_n} = 0.931, 0.971, 0.985$). The fluctuation range of harmonics is 0.14 ± 0.08 and the average deviation of measurement amplitude is $\delta_a = 0.038$.

In the six-modes experiment, the initial amplitude of the OAM modes with $l = 2, 4, 6, 8, 10, 13$ are set to $a_{l_n} = 1, 1.3, 1, 1, 1, 1$. From Fig. 3(c), the initial amplitude distribution can be obtained ($a'_{l_n} = 1.070, 1.297, 0.925, 0.907, 0.900, 0.928$). The fluctuation range of harmonics is 0.18 ± 0.06 and the average deviation of measurement intensity is $\delta_a = 0.07$.

From the three experiments, it is indicated that the average deviation of measurement intensity increases with the increase in the number of superimposed OAM modes.

C. Measurement of OAM phase spectrum

Our proposed measurement scheme can also obtain the initial OAM phase distribution. The experimental results are shown in Fig. 5, where Fig. 5(a) shows the initial OAM phase distribution of two OAM modes. Figure 5(b) shows the initial OAM phase distribution of three OAM modes. Figure 5(c) shows the initial OAM phase distribution of six OAM modes.

In the two-modes experiment, the OAM modes consist of two modes ($l = 3, 8$), and their initial phases

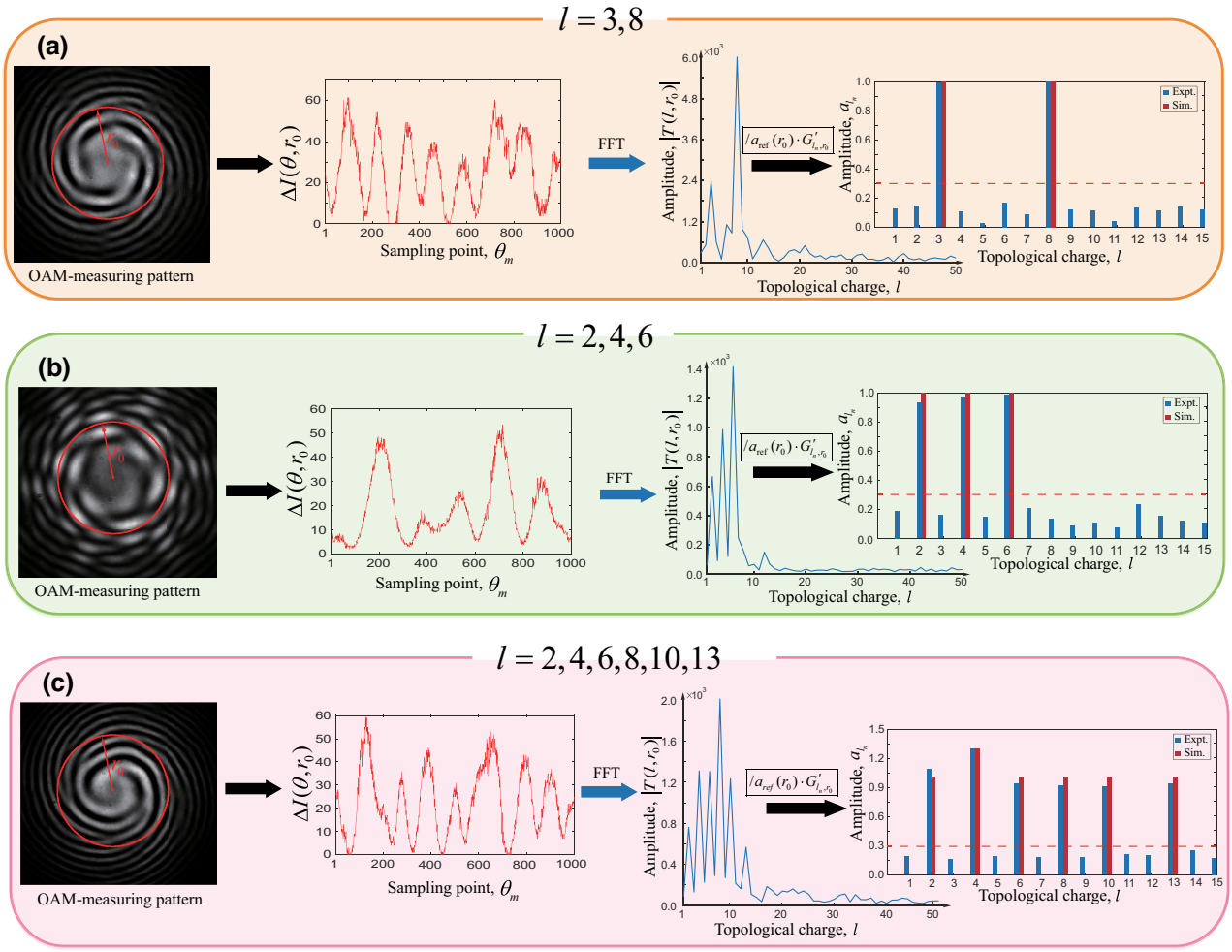

FIG. 4. The experimental process for measuring the OAM amplitude spectrum. (a) The measurement OAM amplitude spectrum of two superimposed OAM modes ($l = 3, 8$). (b) The measurement OAM amplitude spectrum of three superimposed OAM modes ($l = 2, 4, 6$). (c) The measurement OAM amplitude spectrum of six superimposed OAM modes ($l = 2, 4, 6, 8, 10, 13$). Exp, experiments; Sim, simulation.

are set to $\phi_{l_n} = -\pi, \pi$. Similarly, the OAM phase spectrum should be calibrated. The initial OAM phase distribution can be achieved by using the measuring OAM phase spectrum minus the phase calibration coefficient ($P(l, z)$). According to Fig. 5(a), our proposed scheme can measure the initial OAM phase accurately. The average deviation of the measurement phase is $\delta_\phi = 0.196$.

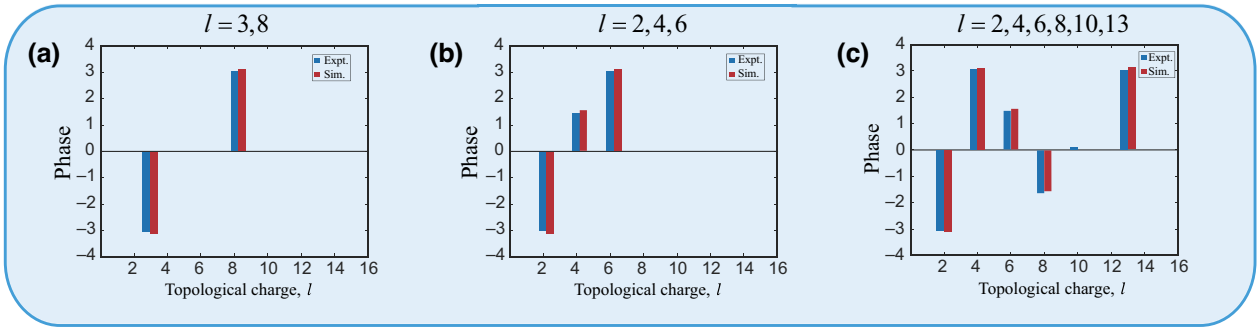

FIG. 5. The experimental results of the initial OAM phase distribution. (a) The initial OAM phase distribution of two superimposed OAM modes ($l = 3, 8$). (b) The initial OAM phase distribution of three superimposed OAM modes ($l = 2, 4, 6$). (c) The initial OAM phase distribution of six superimposed OAM modes ($l = 2, 4, 6, 8, 10, 13$). Exp, experiments; Sim, simulation.

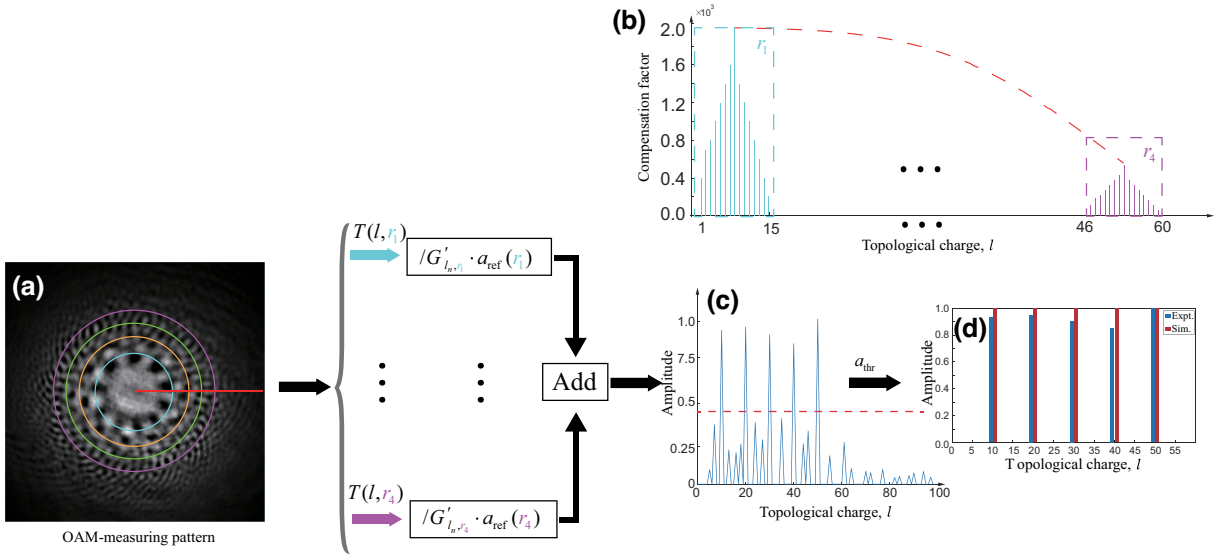

FIG. 6. The method process for enlarging the range of the detectable OAM modes. (a) The OAM-measuring pattern with different topological charges ($l = 10, 20, 30, 40, 50$). (b) The compensation factor. (c) The superimposed OAM amplitude spectrum. (d) The initial OAM amplitude distribution. Exp, experiments; Sim, simulation.

In the three-modes experiment, the OAM modes consist of three modes ($l = 2, 4, 6$), and their initial phases are set to $\phi_{l_n} = -\pi, \pi/2, \pi$. The measurement results are shown in Fig. 5(b) and the average deviation of the measurement phase is $\delta_\phi = 0.266$.

In the six-modes experiment, the OAM modes consist of six modes ($l = 2, 4, 6, 8, 10, 13$), and their initial phases are set to $\phi_{l_n} = -\pi, \pi, \pi/2, -\pi/2, 0, \pi$. The measurement results are shown in Fig. 5(c) and the average deviation of the measurement phase is $\delta_\phi = 0.308$.

IV. DISCUSSION

A. Enlarging the range of detectable OAM modes

According to the Laguerre-Gaussian mode and Eq. (2), the range of detectable OAM modes is finite by using the single measurement radius. Hence, multiple measurement radii are utilized and their OAM complex spectra are spliced together to enlarge the range of detectable OAM modes.

Figure 6 shows the method process for enlarging the range of detectable OAM modes. We design an OAM-multiplexing beam as the input OAM beam, which consists of five OAM modes ($l = 10, 20, 30, 40, 50$). The initial amplitudes are set to $(1, 1, 1, 1, 1)$ and the phase is set to zero for simplicity. The OAM-measuring pattern of this input OAM beam is shown in Fig. 6(a). The four measurement radii ($r_1 = 60$, $r_2 = 85$, $r_3 = 105$, and $r_4 = 125$ pixels) are selected to measure the OAM amplitude spectrum. As indicated by Eq. (12), both the amplitude calibration coefficient ($G_{l_n,r}$) and the reference beam amplitude ($a_{\mathrm{ref}}(r)$) have impacts on the recovery of the initial amplitude, and they vary with the radius. As a result, the compensation factor ($G_{l_n,r}a_{\mathrm{ref}}(r)$), which can be defined as the amplitude calibration coefficients multiplied by the corresponding reference beam amplitude at different radii, is presented in Fig. 6(b).

To enlarge the range of detectable OAM modes, the proposed method consists of four main steps. In the first step, the intensities collected at the four selected measurement radii are transformed by FFT to obtain four OAM amplitude spectra. In the second step, each OAM amplitude spectrum is divided by its corresponding compensation factor, which is the product of the amplitude calibration coefficient ($G'_{l_n,r}$) and the reference beam amplitude ($a_{\mathrm{ref}}(r)$) at each measurement radius. The compensation factors are shown in Fig. 6(b). In the third step, the four OAM complex spectra are added and the superimposed OAM amplitude spectrum can be shown in Fig. 6(c). Finally, by applying a threshold ($a_{\mathrm{thr}} = 0.45$), the initial OAM amplitude distribution can be obtained, as shown in Fig. 6(d).

From Fig. 6(d), it is shown that the input OAM modes can be extracted accurately and the measurement amplitude distributions agree well with the theoretical calculations. The average deviation of the measurement amplitude is 0.112. However, compared with the single measurement radius, the amplitudes of harmonics are obvious. The main reason is that the addition step also superposes the harmonics.

B. Analyzing the effect of optical alignment

Optical alignment has two impacts on measurement results in terms of accuracy. On the one hand, the reference beam and measurement beam need to be radially aligned to

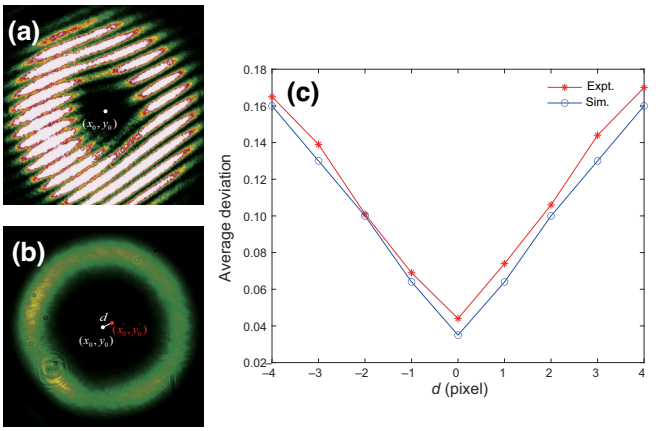

FIG. 7. Analyzing the effect of axial alignment. (a) The OAM-interferential pattern ($d = 10$ pixels and $l = 4$). (b) The OAM-primitive pattern with single OAM mode. (c) The simulation and experimental results for the average deviation of OAM amplitude measurement with different central positions. Exp, experiments; Sim, simulation.

achieve coaxial interference. In our experiment, exceeding a distance of 4 pixels between the center of the measured beam and the center of the reference beam will result in the absence of coaxial interference. As an illustration, for the single OAM mode with $l = 4$, a difference of 6 pixels between the centers of the two beams would yield significantly incorrect measurement results, as demonstrated in Fig. 7(a)(without the appearance of petal-like speckles).

On the other hand, the alignment of pixel (x_0, y_0) relative to the central position of the OAM-measuring pattern also has a significant impact on the measurement results. The single OAM mode is used to find out the central position (x_0', y_0'), which can be shown in Fig. 7(b). To evaluate the effect of central alignment difference ($d = \sqrt{(x_0 - x_0')^2 + (y_0 - y_0')^2}$) on OAM amplitude measurement accuracy, the simulation and experimental results for the average deviation of OAM amplitude measurement are obtained for different central alignment differences (d) ranging from -4 to 4 pixels, as shown in Fig. 7(c). The results indicate that the average deviation increases as the central alignment difference increases.

C. Analyzing the impact of superimposed OAM modes on measurement accuracy

While the superimposed OAM modes can provide significant benefits for OAM-based applications, such as improving efficiency, they can also introduce measurement deviations with the increase of the number of superimposed OAM modes, which are shown in Fig. 8. The results also include a comparison with a deep-learning-based approach [27]. From Fig. 8, the experimental results indicate that the average deviation increases with an increase in the number of superimposed OAM modes. A comparison with the deep-learning-based approach shows that the

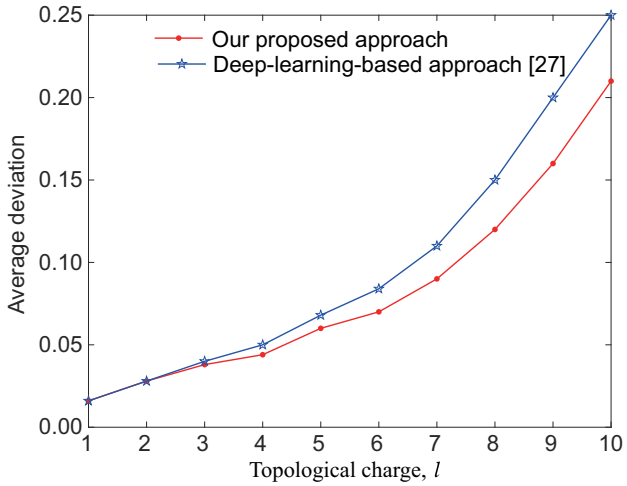

FIG. 8. The average deviation with different numbers of superimposed OAM modes.

increase in superimposed OAM modes has a greater impact on the performance of the deep-learning-based approach.

V. CONCLUSIONS

In summary, we have presented a novel approach for measuring the orbital angular momentum (OAM) complex spectrum of light using the FFT. By coaxially interfering the input OAM light with a Gaussian reference beam, we obtain the intensity distribution of the interference, from which the intensity distribution of the input OAM light is then subtracted to obtain the OAM complex spectrum via FFT. From the calibration coefficient, our experimental results demonstrate accurate measurement of different superimposed OAM modes and their amplitude and phase distributions. Moreover, we have proposed a method for enlarging the detectable range of OAM modes from 1 to 50. Our study also highlights the importance of optical alignment and the number of superimposed OAM modes for accurate measurements. Our proposed scheme offers a promising solution for measuring the OAM complex spectrum and has potential applications in OAM-based communication and some other OAM-based systems.

ACKNOWLEDGMENTS

The work is supported by the National Natural Science Foundation of China (61871234), the Natural Science Foundation of Suqian (K202209), the Postgraduate Research & Practice Innovation Program of Jiangsu Province (KYCX21-0745) and the Open Research Fund of National Laboratory of Solid State Microstructures under Grant No. 36055.

[1] L. Allen, M. W. Beijersbergen, R. J. C. Spreeuw, and J. P. Woerdman, Orbital angular momentum of light and the

transformation of Laguerre-Gaussian laser modes, Phys. Rev. A **45**, 8185 (1992).
[2] V. Y. Bazhenov, M. Vasnetsov, and M. Soskin, Laser beams with screw dislocations in their wavefronts, JETP Lett. **52**, 429 (1990).
[3] N. Heckenberg, R. McDuff, C. Smith, H. Rubinsztein-Dunlop, and M. Wegener, Laser beams with phase singularities, Opt. Quantum Electron. **24**, S951 (1992).
[4] M. Harris, C. Hill, and J. Vaughan, Optical helices and spiral interference fringes, Opt. Commun. **106**, 161 (1994).
[5] X. Fang, H. Ren, and M. Gu, Orbital angular momentum holography for high-security encryption, Nat. Photonics **14**, 102 (2020).
[6] S. Zhao, L. Wang, L. Zou, L. Gong, W. Cheng, B. Zheng, and H. Chen, Both channel coding and wavefront correction on the turbulence mitigation of optical communications using orbital angular momentum multiplexing, Opt. Commun. **376**, 92 (2016).
[7] J. Wang, J. Liu, S. Li, Y. Zhao, J. Du, and L. Zhu, Orbital angular momentum and beyond in free-space optical communications, Nanophotonics **11**, 645 (2022).
[8] D. Yang, Z.-D. Hu, S. Wang, and Y. Zhu, Influence of random media on orbital angular momentum quantum states of optical vortex beams, Phys. Rev. A **105**, 053513 (2022).
[9] J. Zhu, L. Wang, and S. Zhao, Orbital angular momentum multiplexing holography for data storage, IEEE Photonics Technol. Lett. **35**, 179 (2022).
[10] W. Li and S. Zhao, Generation of two-photon orbital-angular-momentum entanglement with a high degree of entanglement, Appl. Phys. Lett. **114**, 041105 (2019).
[11] J. Zhu, L. Wang, J. Ji, and S. Zhao, Real-time measurement of dynamic micro-displacement and direction using light's orbital angular momentum, Appl. Phys. Lett. **120**, 251104 (2022).
[12] G. Verma and G. Yadav, Compact picometer-scale interferometer using twisted light, Opt. Lett. **44**, 3594 (2019).
[13] A. Forbes, A. Dudley, and M. McLaren, Creation and detection of optical modes with spatial light modulators, Adv. Opt. Photonics **8**, 200 (2016).
[14] C. Schulze, S. Ngcobo, M. Duparré, and A. Forbes, Modal decomposition without a priori scale information, Opt. Express **20**, 27866 (2012).
[15] J. Leach, M. J. Padgett, S. M. Barnett, S. Franke-Arnold, and J. Courtial, Measuring the Orbital Angular Momentum of a Single Photon, Phys. Rev. Lett. **88**, 257901 (2002).
[16] J. Leach, J. Courtial, K. Skeldon, S. M. Barnett, S. Franke-Arnold, and M. J. Padgett, Interferometric Methods to Measure Orbital and Spin, or the Total Angular Momentum of a Single Photon, Phys. Rev. Lett. **92**, 013601 (2004).
[17] W. Zhang, Q. Qi, J. Zhou, and L. Chen, Mimicking Faraday Rotation to Sort the Orbital Angular Momentum of Light, Phys. Rev. Lett. **112**, 153601 (2014).
[18] H. Zhou, L. Shi, X. Zhang, and J. Dong, Dynamic interferometry measurement of orbital angular momentum of light, Opt. Lett. **39**, 6058 (2014).
[19] K. Yamane, Z. Yang, Y. Toda, and R. Morita, Frequency-resolved measurement of the orbital angular momentum spectrum of femtosecond ultra-broadband optical-vortex pulses based on field reconstruction, New J. Phys. **16**, 053020 (2014).
[20] G. Kulkarni, R. Sahu, O. S. Magaña-Loaiza, R. W. Boyd, and A. K. Jha, Single-shot measurement of the orbital-angular-momentum spectrum of light, Nat. Commun. **8**, 1 (2017).
[21] Q. Zhao, M. Dong, Y. Bai, and Y. Yang, Measuring high orbital angular momentum of vortex beams with an improved multipoint interferometer, Photonics Res. **8**, 745 (2020).
[22] G. C. G. Berkhout, M. P. J. Lavery, J. Courtial, M. W. Beijersbergen, and M. J. Padgett, Efficient Sorting of Orbital Angular Momentum States of Light, Phys. Rev. Lett. **105**, 153601 (2010).
[23] G. C. Berkhout, M. P. Lavery, M. J. Padgett, and M. W. Beijersbergen, Measuring orbital angular momentum superpositions of light by mode transformation, Opt. Lett. **36**, 1863 (2011).
[24] M. Mirhosseini, M. Malik, Z. Shi, and R. W. Boyd, Efficient separation of the orbital angular momentum eigenstates of light, Nat. Commun. **4**, 1 (2013).
[25] R. Sahu, S. Chaudhary, K. Khare, M. Bhattacharya, H. Wanare, and A. K. Jha, Angular lens, Opt. Express **26**, 8709 (2018).
[26] J. Wang, S. Fu, Z. Shang, L. Hai, and C. Gao, Adjusted EfficientNet for the diagnostic of orbital angular momentum spectrum, Opt. Lett. **47**, 1419 (2022).
[27] H. Guo, X. Qiu, and L. Chen, Simple-Diffraction-Based Deep Learning to Reconstruct a High-Dimensional Orbital-Angular-Momentum Spectrum via Single-Shot Measurement, Phys. Rev. Appl. **17**, 054019 (2022).
[28] H.-L. Zhou, D.-Z. Fu, J.-J. Dong, P. Zhang, D.-X. Chen, X.-L. Cai, F.-L. Li, and X.-L. Zhang, Orbital angular momentum complex spectrum analyzer for vortex light based on the rotational Doppler effect, Light: Sci. Appl. **6**, e16251 (2017).
[29] A. D'Errico, R. D'Amelio, B. Piccirillo, F. Cardano, and L. Marrucci, Measuring the complex orbital angular momentum spectrum and spatial mode decomposition of structured light beams, Optica **4**, 1350 (2017).
[30] S. Fu, Y. Zhai, J. Zhang, X. Liu, R. Song, H. Zhou, and C. Gao, Universal orbital angular momentum spectrum analyzer for beams, PhotoniX **1**, 1 (2020).
[31] E. Karimi, L. Marrucci, C. de Lisio, and E. Santamato, Time-division multiplexing of the orbital angular momentum of light, Opt. Lett. **37**, 127 (2012).
[32] P. Bierdz, M. Kwon, C. Roncaioli, and H. Deng, High fidelity detection of the orbital angular momentum of light by time mapping, New J. Phys. **15**, 113062 (2013).
[33] S. Fu, S. Zhang, T. Wang, and C. Gao, Measurement of orbital angular momentum spectra of multiplexing optical vortices, Opt. Express. **24**, 6240 (2016).
[34] M. Padgett, J. Arlt, N. Simpson, and L. Allen, An experiment to observe the intensity and phase structure of Laguerre–Gaussian laser modes, Am. J. Phys. **64**, 77 (1996).
[35] A. Lyons, T. Roger, N. Westerberg, S. Vezzoli, C. Maitland, J. Leach, M. J. Padgett, and D. Faccio, How fast is a twisted photon?, Optica **5**, 682 (2018).
[36] H. D. Luke, The origins of the sampling theorem, IEEE Commun. Mag. **37**, 106 (1999).